1

2 **Main Manuscript for**

3 Rapid cloud removal of dimethyl sulfide oxidation products limits SO_2
4 and cloud condensation nuclei production in the marine atmosphere

5 Gordon A. Novak[1,#], Charles H. Fite[2], Christopher D. Holmes[2], Patrick R. Veres[3], J. Andrew
6 Neuman[3,4], Ian Faloona[5], Joel A. Thornton[6], Glenn M. Wolfe[7], Michael P. Vermeuel[1,$], Christopher
7 M. Jernigan[1], Jeff Peischl[3,4], Thomas B. Ryerson[3,%], Chelsea R. Thompson[3,4], Ilann Bourgeois[3,4],
8 Carsten Warneke[3,4], Georgios I. Gkatzelis[3,4,^], Mathew M. Coggon[3,4], Kanako Sekimoto[8], T. Paul
9 Bui[9], J. Dean-Day[10], Glenn S. Diskin[11], Joshua P. DiGangi[11], John B. Nowak[11], Richard H. Moore[11],
10 Elizabeth B. Wiggins[11], Edward L. Winstead[11], Claire Robinson[11], Lee Thornhill[11], Kevin J.
11 Sanchez[11], Samuel R. Hall[12], Kirk Ullmann[12], Maximilian Dollner[13], Bernadett Weinzierl[13], Donald
12 Blake[14], and Timothy H. Bertram[1,*]

13 [1]Department of Chemistry, University of Wisconsin – Madison, Madison, WI 53706
14 [2]Department of Earth, Ocean, and Atmospheric Science, Florida State University, Tallahassee, FL
15 32306
16 [3]NOAA Chemical Sciences Laboratory (CSL), Boulder, CO 80305
17 [4]Cooperative Institute for Research in Environmental Sciences, University of Colorado Boulder,
18 Boulder, CO 80305
19 [5]Department of Land, Air and Water Resources, University of California Davis, Davis, CA 95616
20 [6]Department of Atmospheric Science, University of Washington, Seattle, WA 98195
21 [7]Atmospheric Chemistry and Dynamics Lab, NASA Goddard Space Flight Center, Greenbelt, MD
22 20771
23 [8] Yokohama City University, 2360027 Yokohama Kanagawa, Japan
24 [9] NASA Ames Research Center, Mountain View, CA 94035
25 [10] Bay Area Environment Research Institute, Moffett Field, CA 94035
26 [11]NASA Langley Research Center, Hampton, VA 23681
27 [12]NCAR Atmospheric Chemistry Observations and Modeling Laboratory, Boulder, CO 80301
28 [13] University of Vienna, Faculty of Physics, Aerosol Physics and Environmental Physics, 1090
29 Vienna, Austria
30 [14]Department of Chemistry, University of California - Irvine, Irvine, CA 92617
31
32 # Now at Cooperative Institute for Research in Environmental Sciences, University of Colorado
33 Boulder, Boulder, CO and NOAA Chemical Sciences Laboratory (CSL), Boulder, CO 80305
34 $ Now at Department of Soil, Water, and Climate, University of Minnesota – Twin Cities, St. Paul,
35 MN, USA, 55108
36 % Now at Scientific Aviation, Boulder, CO 80301

37   ^Now at Institute of Energy and Climate Research, IEK-8: Troposphere, Forschungszentrum Jülich
38   GmbH, 52428 Jülich, Germany

40   *** Corresponding Author:** Timothy H. Bertram, 1101 University Ave., Madison, WI 53706. Phone:
41   608-890-3422

42   **Email:** timothy.bertram@wisc.edu

43   **Author Contributions:** G.A.N., C.H.F., C.D.H., P.R.V., T.B.R., I.F., and T.H.B. designed research;
44   G.A.N., C.H.F., C.D.H., P.R.V., J.A.N., I.F., G.M.W., M.P.V., C.M.J., J.P., T.B.R., C.R.T., I.B., C.W.,
45   G.I.G., M.M.C, K.S., T.P.B., J.D.D., G.S.D., J.P.D., J.B.N., R.H.M, E.B.W., E.L.W., C.R., L.T.,
46   K.J.S., S.R.H, K.U., M.D., B.W., D.B., and T.H.B performed research; G.A.N., C.H.F., C.D.H.,
47   P.R.V., J.A.N., I.F., G.M.W., M.P.V., C.M.J., J.P., T.B.R., C.R.T., I.B., C.W., G.I.G., M.M.C, K.S.,
48   T.P.B., J.D.D., G.S.D., J.P.D., J.B.N., R.H.M, E.B.W., E.L.W., C.R., L.T., K.J.S., S.R.H, K.U., M.D.,
49   B.W., D.B., and T.H.B analyzed data; G.A.N., C.H.F., C.D.H., and T.H.B. wrote the paper. All
50   authors reviewed, edited, and revised the paper.

51   **Competing Interest Statement:** The authors declare no competing interests.

52   **Classification:** Physical Sciences - Earth, Atmospheric, and Planetary Sciences

53   **Keywords:** dimethyl sulfide, cloud condensation nuclei, sulfate aerosol, marine sulfur, cloud
54   processing

55   **This PDF file includes:**

56   Main Text
57   Figures 1 to 5
58

Abstract

Oceans emit large quantities of dimethyl sulfide (DMS) to the marine atmosphere. The oxidation of DMS leads to the formation and growth of cloud condensation nuclei (CCN) with consequent effects on Earth's radiation balance and climate. Quantitative assessment of the impact of DMS emissions on CCN concentrations necessitates a detailed description of the oxidation of DMS in the presence of existing aerosol particles and clouds. In the unpolluted marine atmosphere, DMS is efficiently oxidized to hydroperoxymethyl thioformate (HPMTF), a stable intermediate in the chemical trajectory towards sulfur dioxide (SO_2) and ultimately sulfate aerosol (Veres et al. 2020). Using direct airborne flux measurements, we demonstrate that irreversible loss of HPMTF to clouds in the marine boundary layer determines the HPMTF lifetime (τ_{HPMTF} < 2 hours) and terminates DMS oxidation to SO_2 in the cloudy marine boundary layer. When accounting for HPMTF cloud loss in a global chemical transport model, we show that SO_2 production from DMS is reduced by 35% globally and near surface (0-3km) SO_2 concentrations over the ocean are lowered by 24%. This large, previously unconsidered loss process for volatile sulfur accelerates the timescale for conversion of DMS to sulfate, while limiting new particle formation in the marine atmosphere and changing the dynamics of aerosol growth. This loss process potentially reduces the spatial scale over which DMS emissions contribute to aerosol production and growth and weakens the link between DMS emission and marine CCN production with subsequent implications for cloud formation, radiative forcing, and climate.

Significance Statement

Ocean emissions of dimethyl sulfide (DMS) are a major precursor for the production and growth of aerosol particles, which can act as seeds for the formation of cloud droplets in the marine atmosphere with subsequent impacts on Earth's climate. Global aircraft observations indicate that DMS is efficiently oxidized to hydroperoxymethyl thioformate (HPMTF), a previously unrecognized molecule, which necessitates revisiting DMS oxidation chemistry in the marine atmosphere. We show through ambient observations and global modelling that a dominant loss pathway for HPMTF is uptake into cloud droplets. This loss process short circuits gas phase oxidation and significantly alters the dynamics of aerosol production and growth in the marine atmosphere.

Main Text

Introduction

Oceanic emission of dimethyl sulfide (DMS; CH_3SCH_3) is the largest natural source of reduced sulfur to the atmosphere (1, 2). The oxidation of DMS ultimately leads to the production of sulfuric acid (H_2SO_4) and methane sulfonic acid (CH_3SO_3H; MSA), which contribute to new particle formation and growth (3–6). Direct observations of the full suite of DMS oxidation products are limited, making it challenging to interpret the large variability in estimates of global sulfur dioxide (SO_2) yields ($31 - 98\%$), where SO_2 is an immediate precursor to sulfate aerosol (SO_4^{2-}) (3, 7). An incomplete representation of DMS oxidation in global models contributes to uncertainty in estimates of the impact of DMS emissions on cloud condensation nuclei (CCN) and climate (7–9), the utility of ice core records of MSA as proxies for historical sea ice extent (10–12), and the use of MSA-to-sulfate ratios (13) as a proxy of pre-industrial temperature and sulfur emissions (14). Uncertainties in the budget of pre-industrial aerosols, including those from DMS oxidation, are the largest source of uncertainty in current estimates of radiative forcing caused by the aerosol indirect effect (9).

The recent discovery of hydroperoxymethyl thioformate ($HOOCH_2SCHO$; HPMTF), a globally ubiquitous DMS oxidation product, necessitates revisiting DMS oxidation mechanisms (15–17). HPMTF is produced by isomerization of the methylthiomethylperoxy radical ($CH_3SCH_2OO\bullet$) which is the primary product of DMS hydrogen abstraction by OH. This isomerization process competes with bimolecular chemistry of $CH_3SCH_2OO\bullet$ which produces SO_2 at high yield. Veres et al. (2020) determined that HPMTF is a dominant oxidation product of DMS, yet the atmospheric fate of

3

107 HPMTF was unknown. Here, using direct airborne eddy covariance (EC) flux measurements, we
108 constrain the chemical fate of HPMTF in the marine boundary layer (MBL). In the cloudy MBL, we
109 demonstrate that the lifetime of HPMTF from cloud loss ($\tau_{HPMTF,cloud}$) is less than two hours and is
110 the dominant HPMTF loss pathway, thus limiting the production of SO_2. In the cloud-free MBL,
111 HPMTF is oxidized by OH forming SO_2, which can continue along the oxidation trajectory toward
112 H_2SO_4 and ultimately CCN production. Low altitude clouds cover nearly 50% of the global oceans
113 in the annual mean, with stratus and stratocumulus alone covering about 35% of the oceans (18).
114 In some regions, like the eastern subtropical oceans, stratus and stratocumulus coverage reaches
115 60% (19). Given that low level clouds are a persistent feature of the marine atmosphere, it is likely
116 that cloud loss of soluble species within the MBL is a significant component of reactive trace gas
117 budgets. To assess the global significance of HPMTF cloud loss on marine sulfur chemistry, we
118 use a global atmospheric chemical transport model with a newly developed method of incorporating
119 cloud chemistry, which accounts for the entrainment of gases into clouds and fractional cloud cover
120 in the chemical rate expression (18).

121 **Results and Discussion**

122 **Airborne flux observations reveal efficient cloud loss of HPMTF**

123 *In situ* airborne observations of HPMTF mixing ratios and vertical fluxes were acquired during the
124 NASA Atmospheric Tomography (ATom) and Student Airborne Research Program 2019 (SARP)
125 missions on the NASA DC-8 research aircraft. Here we focus our analysis on two representative
126 flights: 1) a SARP flight, conducted off the coast of Southern California, within a stratocumulus
127 cloud topped MBL on July 17th 2019, and 2) an ATom-4 flight, conducted over the South Pacific
128 Ocean, within a cloud-free MBL on May 1st, 2018. **Figure 1** shows vertical profiles of DMS and
129 HPMTF mixing ratios, true color satellite imagery and flight tracks during the ATom and SARP MBL
130 measurements. Two salient features emerge in the vertical profiles in DMS and HPMTF: 1) for the
131 cloudy SARP flight, complete depletion of HPMTF is observed from cloud base (360 m) to the top
132 of the MBL (560 m) whereas DMS is well mixed throughout the MBL, and 2) the mean
133 [HPMTF]/[DMS] ratio measured below cloud during SARP (0.05 ± 0.03 mol mol^{-1}) is significantly
134 smaller than that measured in the cloud free MBL during ATom (0.8 ± 0.5 mol mol^{-1}), for comparable
135 solar zenith angles (25.8° ± 2.5 and 21.2° ± 7.1, respectively). This suggests either enhanced
136 HPMTF loss (L_{HPMTF}) or suppressed HPMTF production (P_{HPMTF}) due to lower OH concentrations
137 in the cloudy MBL. Changes in [OH] below cloud are unlikely to explain this difference, as modeled
138 [OH] is reduced by only 30% below cloud, and a reduction in P_{HPMTF} would be partially offset by a
139 reduction in L_{HPMTF} from reactions with OH (see supplemental Table S5 for a full list of reactions
140 contributing to HPMTF production and loss). Nitric oxide (NO) mixing ratios were similar between
141 the regions (8 ppt during the clear-sky ATom flight and 7 ppt during the cloudy SARP flight)
142 indicating that the bimolecular chemistry which competes with HPMTF formation was comparable.
143 We therefore expect the difference in [HPMTF]/[DMS] to be driven by a large additional L_{HPMTF} in
144 the cloudy MBL case.

145 True color satellite imagery (**Fig. 1c**) and forward-facing camera footage (**Fig. S1**) during
146 the SARP flight reveal semi-organized horizontal convective roll structures in the stratocumulus-
147 topped MBL, visible as cloud streets with a period of *ca.* 7 km. This mesoscale convective structure
148 is a common feature of marine stratocumulus systems and is characterized by counter-rotating
149 horizontal vortices generating updrafts where the clouds form and downdrafts of cloud-processed
150 air between, shown schematically in **Fig. 2a** (19, 20). This structure is reflected in the time series
151 (**Fig. 2b**) of both shortwave radiation (here shown as the photolysis rate of ozone, J_{O3}) and the
152 vertical wind speed (*w*), where J_{O3} is enhanced in the cloud free regions and *w* is negative
153 (indicating a downdraft). The impact of the convective structure is clearly distinguishable in HPMTF,
154 which is depleted in the downdrafts where the air has recently passed through a cloud, indicative
155 of irreversible HPMTF loss to cloud droplets (**Fig. 2c**). Based on the response of [HPMTF] to
156 overhead clouds shown in **Fig. 2c**, we expect aircraft measurements of the vertical flux of HPMTF
157 to be positive in spite of the absence of an entrainment flux at cloud top due to the negligible

158 difference in concentration between the MBL top and overlying free troposphere, and the negative
159 flux at the surface due to dry deposition. The contribution of convective roll structures on new
160 particle formation (21) and surface heat and momentum fluxes have been demonstrated previously
161 (19, 20), but the influence of these boundary layer dynamics on the concentration and vertical
162 transport of reactive chemical species have not previously been considered. Observations from
163 high time response in situ airborne instruments, provide a unique opportunity to quantitatively
164 determine the loss rate of soluble reactive gases to clouds.

165   Vertical fluxes of HPMTF during SARP were directly determined in the stratocumulus
166 topped MBL at three altitudes (170, 180, and 255 m) using the eddy covariance (EC) technique
167 with the Continuous Wavelet Transform (CWT) method described further in the Materials section
168 and the Supplemental text. Mean ($\pm 1\sigma$) HPMTF mixing ratios for these segments were 4.1 ± 1.7,
169 4.4 ± 1.8, and 3.7 ± 1.7 parts per trillion (ppt) respectively. Observed HPMTF vertical fluxes (F_{HPMTF})
170 at each altitude were 0.20 ± 0.05, 0.23 ± 0.09, and 0.20 ± 0.05 ppt m s^{-1}. For comparison, the
171 HPMTF surface flux (-0.04 ppt m s^{-1}, where a negative flux indicates deposition), was calculated
172 from the mean MBL [HPMTF] and the average wind speed adjusted surface deposition velocity
173 measured from Scripps Pier, La Jolla CA (22) discussed further in SI S4. The large, positive fluxes
174 measured at flight altitude together with the low HPMTF mixing ratios implies a significant overhead
175 HPMTF loss process. The measured flux cannot be sustained by entrainment from the free
176 troposphere as [HPMTF] is near zero in both the free troposphere and the cloudy fraction at the
177 top of the MBL leading to a negligible free tropospheric entrainment flux for HPMTF. The vertical
178 profile of the mixing ratio normalized flux (F_{HPMTF}/[HPMTF]) shown in **Fig. 3c** highlights the process
179 difference in loss rates aloft between the cloudy and clear sky cases. In the stratocumulus topped
180 MBL, extrapolation of the linear flux profile to cloud base (z_{cb}) permits calculation of an exchange
181 velocity (v_{ex}) between the sub-cloud (sc) and cloud filled regions of the MBL ($F_{HPMTF,z_{cb}} \times$
182 $([HPMTF]_{sc} - [HPMTF]_{cld})^{-1} = v_{ex} = 8.6$ cm s^{-1}), where the HPMTF concentration in the cloud
183 filled region ([HPMTF]$_{cld}$) is near zero. Linear extrapolation of the flux profile is justified as the
184 chemical production and loss terms of HPMTF are constant in the well mixed boundary layer,
185 meaning only the exchange terms at the ocean surface and cloud base boundaries control the
186 shape of the flux profile. The cloud base flux ($F_{HPMTF,z_{cb}}$) is a measure of the net flux across the
187 cloud base, and therefore includes any potential HPMTF flux term from evaporation of cloud
188 droplets turbulently mixed into the sub-cloud region from the cloud layer.

189   Our observations indicate that HPMTF is strongly depleted in cloud-processed air. For
190 highly soluble species with irreversible uptake, loss to cloud droplets occurs at the diffusion limit
191 resulting in very short in-cloud lifetimes (<5 s) (23) for typical stratocumulus cloud drop diameters
192 and concentrations (d = 15 μm, N_d = 75 cm^{-3}, (24)). If the average residence time of air within
193 stratocumulus clouds is at least comparable to the in-cloud HPMTF loss rate (18), and HPMTF
194 irreversibly reacts within the cloud droplet, we expect cloud uptake to be a significant term in the
195 HPMTF budget. Uptake of select isoprene derived hydroxy nitrates to liquid aerosol has recently
196 been shown to account for a significant global NO$_x$ sink, demonstrating the importance of water-
197 mediated multiphase chemistry (25). Despite the critical importance of clouds in regulating reactive
198 trace gases, we are not aware of any direct measurements of the loss rate of soluble molecules to
199 stratocumulus clouds in the MBL to constrain the timescales for mixing of an airmass into the cloud
200 layer.

201   Using our airborne flux measurements, we can estimate the mean residence time of MBL
202 air in clouds (T_{cld}) as $T_{cld} = d_{cld} \times (v_{ex})^{-1}$, where d_{cld} is the cloud thickness ($d_{cld} = z_i - z_{cb}$ = 200 m,
203 where z_i is the boundary layer depth, determined from the vertical gradients of potential
204 temperature, wind speed, and mixing ratios of water vapor, DMS, and HPMTF) and v_{ex} is the
205 measured exchange velocity between the sub-cloud and cloud filled regions of the MBL. Using this
206 approach, we derive a mean in-cloud residence time of 0.64 ± 0.33 h. These calculations are largely
207 consistent with estimated stratocumulus residence times in the range of 0.25 to 0.66 h (26–29).
208 Results from a large eddy simulation (LES) coupled to a trajectory-ensemble model found that

209 individual turbulent air parcels within a non-precipitating stratocumulus topped MBL have a modal
210 cloud residence time of 0.25 h (26–29). Similarly, we can calculate the lifetime of HPMTF in the
211 subcloud region with respect to mixing and subsequent loss in the cloud filled region as $\tau_{mix,cld} =$
212 $z_{cb} \times (v_{ex})^{-1}$. Using the measured exchange velocity derived above, we determine $\tau_{mix,cld}$ to be
213 1.2 ± 0.6 h.

214   The vertical flux of HPMTF was also assessed under clear-sky conditions during ATom.
215 We use data from the ATom-4 campaign on May 1st 2018 as a case study due to the high HPMTF
216 mixing ratios and the presence of multiple steady flight legs within the boundary layer which enables
217 analysis of the vertical flux profile. The near-surface vertical structure in this region was comprised
218 of a cloud-free well-mixed turbulent MBL with height of approximately 550 m. At the MBL top there
219 was a weak inversion separating the MBL from a stably stratified buffer layer (BuL) up to a height
220 of 1700 m containing sparse fair weather cumulus clouds, which is a common structure in tropical
221 trade wind regimes (30–32). Mixing time in the BuL has been estimated to be approximately 30
222 hours compared to less than one hour in the well-mixed MBL indicating the two layers are distinct
223 despite the weak inversion separating them (33). HPMTF EC fluxes were calculated for four
224 sequential flux legs (L1-L4) at altitudes of 180, 180, 390, and 570 m respectively, where the 570 m
225 leg was in the bottom of the BuL. Mean HPMTF mixing ratios for all legs ranged between 30 –45
226 ppt. Observed F_{HPMTF} at each altitude were 0.2 ± 0.1, 0.1 ± 0.05, 0.2 ± 0.05, and 0.3 ± 0.1 ppt m s-
227 ^{1}. A clear-sky HPMTF surface flux of -0.33 ppt m s^{-1} was calculated from the mean MBL [HPMTF]
228 and the average scaled surface exchange velocity. We again observe a positive flux at flight
229 altitude, although the much higher [HPMTF] results in a significantly smaller concentration
230 normalized flux ($F_{[HPMTF]}$/[HPMTF]) shown in **Fig. 3c**, with a magnitude consistent with entrainment
231 of air by the buffer layer. Linear extrapolation of the observed flux profile from the surface to the
232 top of the MBL (550 m) yields F_{HPMTF} = 0.6 ppt m s^{-1}, which yields an entrainment rate of air to the
233 BuL ($w_e = \left(F_{HPMTF,z_{zi}} \times (|[HPMTF]_{MBL} - [HPMTF]_{BuL}|)^{-1} = 2.9 \pm 1.4$ cm s^{-1}). This entrainment
234 rate is within the range of 1.0 to 3.5 cm s^{-1} observed in similar trade-wind boundary layers with
235 overlying BuL structures as observed here (31).

236 **Observationally constrained HPMTF budget in the marine boundary layer**

237 To assess the consistency of fast cloud uptake of HPMTF, derived from our flux measurements,
238 with our current understanding of HPMTF production and loss, we use aircraft observations to
239 constrain the HPMTF scalar budget equation (Eq. 1):

240 $$\frac{\partial [HPMTF]}{\partial t} = P - L - A - \frac{d\langle w'[HPMTF]'\rangle}{dz}$$ Eq. 1

241 where the time rate of change in the concentration of HPMTF ($\frac{\partial [HPMTF]}{\partial t}$) is the sum of the net *in situ*
242 chemical production and loss rates of HPMTF (*P and L)*, horizontal advection (*A*), and the vertical
243 flux divergence $\left(\frac{d\langle w'[HPMTF]'\rangle}{dz}\right)$. Integrating Eq. 1 from the surface to cloud base (z_{cb}) and from z_{cb}
244 to the top of the MBL (z_i) results in a coupled pair of HPMTF budget equations Eq. 2a and Eq. 3a
245 where the HPMTF flux at cloud base $\left(F_{HPMTF,z_{cb}} = \langle w'[HPMTF]'\rangle_{z_{cb}} = 0.38 \pm 0.07 \text{ ppt m s}^{-1}\right)$ is
246 common to both equations, as a source to the cloud layer and a loss from the subcloud layer. The
247 HPMTF budget equation for the cloud layer ($z_{cb} < z < z_i$) can be written as:

248 $$\frac{\partial [HPMTF]_{cld}}{\partial t} = P_{cld} - A_{cld} - k_{cld}[HPMTF]_{cld} - k_{OH+HPMTF}[OH]_{cld}[HPMTF]_{cld} + \frac{\langle w'[HPMTF]'\rangle_{cb}}{(z_i-z_{cb})}$$ Eq. 2a

249 Assuming that: 1) [HPMTF] is in steady-state in the cloud layer, a valid assumption given that τ_{cld}
250 < 5s, 2) horizontal advection is negligible, and 3) k_{cld} >>> $k_{OH+HPMTF}$ × [OH]cld, a valid assumption as
251 k_{cld} > 0.2 s^{-1}, we can rewrite Eq. 2a solving for [HPMTF]cld as:

252 $$[HPMTF]_{cld} = (k_{cld})^{-1} \times \left(P_{cld} + \frac{\langle w'[HPMTF]'\rangle_{cb}}{(z_i-z_{cb})}\right)$$ Eq. 2b

253 For [HPMTF]$_{cld}$ to be greater than the CIMS detection limit (<1 ppt), P_{cld} would need to be larger
254 than 700 ppt h^{-1}, a value inconsistent with measured [DMS]$_{cld}$, modeled [OH], and known DMS
255 oxidation kinetics. This confirms the near zero HPMTF concentration measured in cloud.

256 The HPMTF budget equation for the subcloud layer ($z < z_{cb}$) can be written as:

257 $$\frac{\partial [HPMTF]_{sc}}{\partial t} = P_{sc} - A_{sc} - \left(k_{OH+HPMTF}[OH]_{sc} + k_{het} + \frac{v_d}{z_{cb}}\right)[HPMTF]_{sc} - \frac{\langle w'[HPMTF]'\rangle_{cb}}{z_{cb}}$$ Eq. 3a

258 where k_{het} is the rate coefficient for HPMTF loss to aerosol particles. The HPMTF storage term
259 ($\frac{\partial [HPMTF]_{sc}}{\partial t}$) in the sub-cloud region was calculated to be 0 ± 0.2 ppt h^{-1} based on the time rate of
260 change in [HPMTF] from legs 1 and 3 which passed over the same location. On all three sampling
261 legs during SARP, the along flight track component of horizontal advection in [HPMTF] was small
262 ($\frac{\partial [HPMTF]}{\partial x}$ < 0.1 ppt h^{-1}). Due to limitations in the sampling strategy, we cannot constrain the cross-
263 flight track advection term but expect it to be small due to the homogeneity of the coastal ocean
264 sampling region. Taking these two assumptions we can rearrange Eq. 3a to solve for the HPMTF
265 production rate required to balance the HPMTF budget:

266 $$P_{sc} = \left(k_{OH+HPMTF}[OH]_{sc} + k_{het} + \frac{v_d}{z_{cb}}\right)[HPMTF]_{sc} + \frac{\langle w'[HPMTF]'\rangle_{cb}}{z_{cb}}$$ Eq. 3b

267 Concentrations of OH were determined using a 0-D chemical box model constrained by the SARP
268 chemical and meteorological observations as described in SI S5. The model calculated [OH] (3.3
269 ± 1 × 10^6 molecules cm^{-3}) is consistent with prior model calculations of [OH] in the coastal MBL
270 during summer (34, 35). For [HPMTF]$_{sc}$ = 4.4 ± 2.1 ppt, the OH-initiated gas-phase loss of HPMTF
271 is estimated at 0.57 ± 0.28 ppt h^{-1}, assuming that HPMTF reacts with OH at a rate comparable to
272 the structurally similar molecule methyl thioformate (MTF, CH_3SCHO, $k_{OH+CH3SCHO}$ = 1.1 × 10^{-11} cm^3
273 molecule^{-1} s^{-1}), as there is no literature report of OH+HPMTF. The loss rate of HPMTF to aerosol
274 particles (k_{het}) was calculated as $\frac{\gamma \omega S_a}{4}$, where γ is the HMPTF reactive uptake coefficient, ω is the
275 HPMTF mean molecular speed and S_a is the aerosol surface area. At present, γ(HPMTF) for marine
276 aerosol is unknown. If we assume that HPMTF reacts at surfaces at a rate comparable to other
277 soluble reactive gases (γ = 0.01), we predict an HPMTF loss rate to aerosol of 0.14 ± 0.07 ppt h^{-1}
278 for the aerosol surface area concentrations measured below cloud (S_a = 15 μm^2 cm^{-3}). There is
279 also no experimentally measured HPMTF photolysis rate, however the lifetime of the structurally
280 similar molecule MTF to photolysis is 3.7 days at the equator, suggesting photolysis of the HPMTF
281 aldehyde group is a minor loss term (<0.1 ppt h^{-1}) in the scalar budget analysis (36). HPMTF loss
282 *via* deposition to the ocean surface is estimated to be 0.4 ± 0.2 ppt h^{-1}, based on the wind speed
283 dependent deposition velocity (v_d). HPMTF loss to the overhead cloud layer, the final term in Eq.
284 3b is determined to be 3.8 ± 0.7 ppt h^{-1} from the extrapolated flux profile, representing the largest
285 loss term in the HPMTF budget. Note that this term represents the *net* cloud loss flux and therefore
286 includes any potential source of HPMTF from cloud droplet evaporation in the below cloud fraction
287 of the MBL. Collectively, the total HPMTF loss rate and the corresponding HPMTF production rate
288 in the sub-cloud region is estimated to be 4.9 ± 0.8 ppt h^{-1}, where the uncertainty is calculated by
289 propagating the 1σ variance in [HPMTF]$_{sc}$, and the uncertainty in the interpolated flux profile
290 through Eq. 3b.

291 For comparison, we can use aircraft observations to estimate HPMTF *in situ* production
292 from DMS ($P_{sc} = \alpha k_{OH+DMS}[OH][DMS]$), where α is the fraction of the H-abstraction reaction of
293 DMS with OH (k_{OH+DMS} = 4.7 × 10^{-12} cm^3 molecule^{-1} s^{-1}), that yields HPMTF. The α term accounts
294 for the competition between isomerization (that forms HPMTF) and bimolecular chemistry with NO,
295 HO$_2$, and RO$_2$ (calculation of α is described in Supplemental S5). We estimate HPMTF production
296 (P_{HPMTF}) = 4.1 ± 1.0 ppt h^{-1} (α = 0.76, [DMS]$_{obs}$ = 96 ppt, [OH] = 3.3 × 10^6 molecules cm^{-3}). The
297 observationally constrained HPMTF scalar budget and P_{HPMTF} calculated from DMS therefore close

298 to within 1 ppt h^{-1}. If the cloud loss term is not included in the scalar budget analysis, the HPMTF
299 budget does not close to within 3 ppt h^{-1}.

300   This analysis indicates that: 1) rapid cloud loss for HPMTF is required to close the HPMTF
301 budget in the cloud topped MBL, 2) model estimates for $k_{OH+HPMTF}$ (1.1 × 10^{-11} cm^3 molecule^{-1} s^{-1})
302 are likely accurate to within a factor of two, otherwise the SARP and ATom budgets would not
303 close, and 3) cloud uptake dominates the fate of HPMTF in the stratocumulus topped MBL ($\tau_{mix,cld}$ =
304 1.2 h, τ_{chem} > 5 h). A diagram of HPMTF chemical budget terms are shown in **Fig. 4.** Our
305 observations suggest that HPMTF loss to clouds is an irreversible sink for DMS derived sulfur,
306 where HPMTF cloud uptake contributes to cloud droplet mass (likely as SO_4^{2-}) but quenches the
307 potential for new particle formation, damping the link between DMS emissions and CCN
308 concentrations.

309 **Impact of HPMTF cloud loss on global sulfur chemistry**

310 To assess the global significance of HPMTF cloud loss on marine sulfur chemistry, we update the
311 DMS and HPMTF chemistry in the GEOS-Chem chemical transport model (version 12.9.2,
312 www.geos-chem.org), which includes a recently developed method of incorporating cloud uptake
313 in the chemical rate expression (18) and recent updates to marine halogen chemistry (37). Globally,
314 we calculate that 46% of emitted DMS forms HPMTF. Prior observationally constrained box
315 modeling of HPMTF production showed yields of HPMTF from DMS of 38 and 32%, for ATom 3
316 and 4 respectively (15). In prior global modelling of the chemical fate of HPMTF using the CAM-
317 chem chemical transport model, the only HPMTF loss process considered was reaction with OH
318 (15). Using the kinetic rates described in the prior section, we calculate the annual mean fraction
319 of emitted sulfur from DMS, as a function of latitude, that is lost *via* the primary loss pathways (**Fig.
320 5a**). The global mean fraction of DMS-derived sulfur that is lost to clouds as HPMTF is 36%, with
321 zonal means ranging from 10-50%. An additional 15% of HPMTF is lost to aerosol particles,
322 meaning that less than half of the sulfur in HPMTF ultimately forms SO$_2$. During January, when
323 DMS emissions in the Southern Hemisphere are highest, terminal sulfur loss to cloud uptake peaks
324 at 0.58 Gg yr^{-1}, which accounts for 33% of total DMS loss. A sensitivity test taking $k_{OH+HPMTF}$ at an
325 upper limit of 5.5 × 10^{-11} cm^3 molecule^{-1} s^{-1} (5x base rate) shows that 31% of DMS is lost through
326 the HPMTF cloud uptake channel compared to 36% in the base case, suggesting that uncertainty
327 in the OH+HPMTF rate constant has little impact on this analysis.

328   The measurements and global model simulations presented here indicate that cloud uptake of
329 HPMTF is a significant volatile sulfur loss channel, reducing the SO$_2$ production from DMS by 35%
330 globally and lowering near surface (0-3km) SO$_2$ concentrations over the ocean by 24% (**Fig. 5b**),
331 with consequent impacts on new particle formation from the nucleation of sulfuric acid (38). The
332 regions with the largest percent change in SO$_2$ in the western ends of the major ocean gyres are
333 regions where DMS oxidation is both a dominant local source for SO$_2$ and where HPMTF
334 production and subsequent cloud loss are efficient. In non-precipitating clouds, the condensed-
335 phase products of HPMTF aqueous-phase chemistry would contribute to particle mass following
336 cloud processing but would not increase particle number density (4, 39). Importantly, the proposed
337 prompt formation of SO$_4^{2-}$ from aqueous HPMTF cloud chemistry dramatically increases the
338 production rate of SO_4^{2-} in the MBL (by over 500%) and the SO_4^{2-} concentration in the marine lower
339 atmosphere (0-3km) by 22%. While the total global sulfate burden changes only slightly, the
340 acceleration of DMS conversion to SO_4^{2-} leads to a marked shift in the spatial distribution of sulfate
341 in marine environments (**Fig. 5c**) and the temporal connections between DMS emissions and SO$_4^{2-}$
342 formation.

343   The unified approach of direct ambient measurement of cloud uptake rates and global chemical
344 modeling reveals the substantial role of clouds in regulating the budget of volatile organic molecules
345 in the lower troposphere. We expect that cloud uptake contributes significantly to the budgets of a
346 wide array of reactive trace gases in the atmosphere, with consequent impacts on CCN and
347 chemical budgets in cloudy regions across the globe.

Materials and Methods

HPMTF Airborne Observations
Full details of the airborne detection of HPMTF are provided by Veres et al. (2020) with a brief description given here (15). HPMTF mixing ratios were measured on the NASA ATom and SARP campaigns with an iodide-adduct chemical ionization time-of-flight mass spectrometer (iodide CIMS, Aerodyne Research Inc.). Ambient air was sampled through a temperature, pressure, humidity, and mass flow-controlled inlet. Instrument backgrounds were determined by overflowing the inlet with scrubbed ambient air periodically and instrument sensitivity to HPMTF was determined in post-campaign laboratory studies. HPMTF is detected as a stable adduct ion with iodide ($I-C_2H_4O_3S^-$) at a mass-to-charge ratio (m/z) of 234.8931. This mass is not fully resolvable from the detected product ion of dinitrogen pentoxide (N_2O_5) at the mass resolution of the instrument ($m/\Delta m$ = 5000) and data was filtered to remove periods where N_2O_5 potentially contributed to observed HPMTF. We note that the expected contribution of N_2O_5 to the observed HPMTF signal during the flights discussed here is negligible as they took place during daytime under low NO_x conditions where N_2O_5 concentrations are low (<1 ppt). Subsequent to the publication Veres et al. (2020), further evaluation of the calibration method identified a bias in the experiment resulting in an overestimation in the originally reported HPMTF mixing ratios. Revised calibration experiments were performed which removed that source of bias, yielding a corrected instrument calibration factor. A corrigendum to Veres et al. (2020) has been posted detailing the updated calibration factor and the impact of those changes on the ATom observations reported in that work (40). The HPMTF mixing ratios used here for both the SARP and ATom flights reflect the updated HPMTF calibration factor. The updated ATom dataset is available through the Distributed Active Archive Center for Biogeochemical Dynamics (38, https://doi.org/10.3334/ORNLDAAC/1745). The total uncertainty for HPMTF for the ATom observations was 12% + 0.4 ppt, and 1σ precision was 0.3 ppt for 1 s measurements. For the SARP flight HPMTF uncertainty was 12% + 0.8 ppt and 1σ precision was 0.9 ppt. DMS during SARP was measured with a proton transfer time-of-flight mass spectrometer (42). The DMS measurement from ATom used in this analysis was from whole air samples analyzed with gas chromatography (43). Further details of the DMS measurements and other ancillary airborne measurements during ATom and SARP are listed in **Tables S1 and S2**, respectively.

Airborne HPMTF Vertical Flux
The airborne vertical flux of HPMTF was computed using the eddy covariance (EC) technique using the continuous wavelet transform (CWT) method (44–46). CWT methods for computing EC flux have emerged as a powerful technique in airborne flux studies as it does not require homogeneity or stationarity over the averaging period and because it preserves time information, allowing for the computed flux to resolve changes over heterogeneous surfaces (44, 45, 47). All EC flux determinations for HPMTF were performed at 1 Hz time resolution. Standard flux data processing procedures and uncertainty analysis were implemented as described in **SI Appendix S2**. Flux averaging periods were manually selected for periods of stable aircraft altitude, pitch, and roll and to avoid data gaps in the HPMTF measurement as described in **SI Appendix S2.** The SARP flight presented here was the only available flight in the MBL below cloud during the SARP or ATom missions. The ATom-4 May 1st 2018 flight was selected as a clear sky comparison case study because of the similar atmospheric conditions (e.g. SZA, O_3, NO, aerosol surface area) compared to the SARP flight in order to limit differences in HPMTF chemistry between the flights to the presence or absence of clouds.

Global Chemical Transport Model
The chemistry of DMS and its oxidation products, including HPMTF, were simulated using the GEOS-Chem global chemical transport model (version 12.9.2). The model includes comprehensive tropospheric oxidant chemistry, with recent updates to halogen chemistry (37) and cloud processing (18). Simulations were performed at 4° × 5° horizontal resolution with 72 vertical levels. Model sensitivity simulations were run at multiple rate constants for HPMTF + OH. The base model case uses a rate constant of 1.11×10^{-11} cm^3 molec.$^{-1}$ s^{-1}. Additional simulations using HPMTF +

OH of 5.5×10^{-11} cm^3 molec.$^{-1}$ s^{-1} are taken to provide an upper limit case of HPMTF gas phase oxidation by OH which would reduce the significance of HPMTF cloud uptake. A lower limit HPMTF + OH case was simulated using the calculated rate constant of Wu et. al. (2015) of 1.40×10^{-12} cm^3 molec.$^{-1}$ s^{-1} (16). Heterogeneous uptake to both clouds and aerosols was simulated using a reactive uptake coefficient (γ) of 0.01. Model sensitivity simulations were also performed with and without HPMTF heterogeneous uptake to clouds and aerosols. A full description of the GEOS-Chem model implementation, sensitivity simulations, and model comparison to the ATom observations are provided in the **SI Appendix S6-S8**.

Code and Data Availability

Acknowledgments

References

1. M. O. Andreae, Ocean-atmosphere interactions in the global biogeochemical sulfur cycle. *Mar. Chem.* **30**, 1–29 (1990).
2. T. S. Bates, B. K. Lamb, A. Guenther, J. Dignon, R. E. Stoiber, Sulfur emissions to the atmosphere from natural sources. *J. Atmos. Chem.* **14**, 315–337 (1992).
3. E. H. Hoffmann, *et al.*, An advanced modeling study on the impacts and atmospheric implications of multiphase dimethyl sulfide chemistry. *Proc. Natl. Acad. Sci.* **113**, 11776–11781 (2016).
4. A. D. Clarke, *et al.*, Particle production in the remote marine atmosphere: Cloud outflow and subsidence during ACE 1. *J. Geophys. Res. Atmos.* **103**, 16397–16409 (1998).
5. S. Schobesberger, *et al.*, Molecular understanding of atmospheric particle formation from sulfuric acid and large oxidized organic molecules. *Proc Natl Acad Sci U S A* **110**, 17223–17228 (2013).
6. M. Sipila, *et al.*, The role of sulfuric acid in atmospheric nucleation. *Science (80-.).* **327**, 1243–1246 (2010).
7. I. Faloona, Sulfur processing in the marine atmospheric boundary layer: A review and critical assessment of modeling uncertainties. *Atmos. Environ.* **43**, 2841–2854 (2009).
8. P. K. Quinn, T. S. Bates, The case against climate regulation via oceanic phytoplankton sulphur emissions. *Nature* **480**, 51–56 (2011).

451 9. K. S. Carslaw, *et al.*, Large contribution of natural aerosols to uncertainty in indirect
452 forcing. *Nature* **503**, 67–71 (2013).
453 10. M. A. J. Curran, T. D. Van Ommen, V. I. Morgan, K. L. Phillips, A. S. Palmer, Ice core
454 evidence for Antarctic sea ice decline since the 1950s. *Science (80-.).* **302**, 1203–1206
455 (2003).
456 11. E. S. Saltzman, I. Dioumaeva, B. D. Finley, Glacial/interglacial variations in
457 methanesulfonate (MSA) in the Siple Dome ice core, West Antarctica. *Geophys. Res. Lett.*
458 **33**, 1–4 (2006).
459 12. M. B. Osman, *et al.*, Industrial-era decline in subarctic Atlantic productivity. *Nature* **569**,
460 551–555 (2019).
461 13. M. E. Hansson, E. S. Saltzman, The first Greenland ice core record of methanesulfonate
462 and sulfate over a full glacial cycle. *Geophys. Res. Lett.* **20**, 1163–1166 (1993).
463 14. K. A. Read, *et al.*, DMS and MSA measurements in the Antarctic boundary layer: impact
464 of BrO on MSA production. *Atmos. Chem. Phys.* **8**, 2985–2997 (2008).
465 15. P. R. Veres, *et al.*, Global airborne sampling reveals a previously unobserved dimethyl
466 sulfide oxidation mechanism in the marine atmosphere. *Proc. Natl. Acad. Sci. U. S. A.*
467 **117**, 4505–4510 (2020).
468 16. R. Wu, S. Wang, L. Wang, New mechanism for the atmospheric oxidation of dimethyl
469 sulfide. The importance of intramolecular hydrogen shift in a CH3SCH2OO radical. *J.*
470 *Phys. Chem. A* **119**, 112–117 (2015).
471 17. T. Berndt, *et al.*, Fast peroxy radical isomerization and OH recycling in the reaction of OH
472 radicals with dimethyl sulfide. *J. Phys. Chem. Lett.*, 6478–6483 (2019).
473 18. C. D. Holmes, *et al.*, The role of clouds in the tropospheric NOx cycle: a new modeling
474 approach for cloud chemistry and its global implications. *Geophys. Res. Lett.* **46**, 4980–
475 4990 (2019).
476 19. R. Wood, Stratocumulus clouds. *Mon. Weather Rev.* **140**, 2373–2423 (2012).
477 20. G. S. Young, D. a. R. Kristovich, M. R. Hjelmfelt, R. C. Foster, Rolls, streets, waves, and
478 more. *Bull. Am. Meteorol. Soc.* **83**, 1001–1001 (2002).
479 21. J. Lampilahti, *et al.*, Roll vortices induce new particle formation bursts in the planetary
480 boundary layer. *Atmos. Chem. Phys.* **20**, 11841–11854 (2020).
481 22. M. P. Vermeuel, G. A. Novak, C. M. Jernigan, T. H. Bertram, Diel profile of
482 hydroperoxymethyl thioformate: evidence for surface deposition and multiphase
483 chemistry. *Environ. Sci. Technol.* **54**, 12521–12529 (2020).
484 23. S. Z. Levine, S. E. Schwartz, In-cloud and below-cloud scavenging of Nitric acid vapor.
485 *Atmos. Environ.* **16**, 1725–1734 (1982).
486 24. N. L. Miles, J. Verlinde, E. E. Clothiaux, Cloud droplet size distributions in low-level
487 stratiform clouds. *J. Atmos. Sci.* **57**, 295–311 (2000).
488 25. K. T. Vasquez, *et al.*, Rapid hydrolysis of tertiary isoprene nitrate efficiently removes NOx
489 from the atmosphere. *Proc. Natl. Acad. Sci. U. S. A.* **117**, 33011–33016 (2021).
490 26. G. Feingold, S. M. Kreidenweis, Y. Zhang, Stratocumulus processing of gases and cloud
491 condensation nuclei 1. Trajectory ensemble model. *J. Geophys. Res. Atmos.* **103**, 19527–
492 19542 (1998).
493 27. G. Feingold, A. McComiskey, D. Rosenfeld, A. Sorooshian, On the relationship between
494 cloud contact time and precipitation susceptibility to aerosol. *J. Geophys. Res. Atmos.*
495 **118**, 10,544-10,554 (2013).
496 28. B. Stevens, G. Feingold, W. R. Cotton, R. L. Walko, Elements of the microphysical
497 structure of numerically simulated nonprecipitating stratocumulus. *J. Atmos. Sci.* **53**, 980–
498 1006 (1996).
499 29. Y. L. Kogan, Large-eddy simulation of air parcels in stratocumulus clouds: Time scales
500 and spatial variability. *J. Atmos. Sci.* **63**, 952–967 (2006).
501 30. I. Faloona, *et al.*, Sulfur dioxide in the tropical marine boundary layer: dry deposition and
502 heterogeneous oxidation observed during the Pacific Atmospheric Sulfur Experiment. *J.*
503 *Atmos. Chem.* **63**, 13–32 (2010).
504 31. S. A. Conley, *et al.*, Closing the dimethyl sulfide budget in the tropical marine boundary
505 layer during the Pacific Atmospheric Sulfur Experiment. *Atmos. Chem. Phys.* **9**, 8745–

506   8756 (2009).

507   32.   L. M. Russell, *et al.*, Bidirectional mixing in an ACE 1 marine boundary layer overlain by a
508   second turbulent layer. *J. Geophys. Res. Atmos.* **103**, 16411–16432 (1998).

509   33.   A. Bandy, *et al.*, Pacific Atmospheric Sulfur Experiment (PASE): Dynamics and chemistry
510   of the south Pacific tropical trade wind regime. *J. Atmos. Chem.* **68**, 5–25 (2011).

511   34.   T. P. Riedel, *et al.*, Nitryl chloride and molecular chlorine in the coastal marine boundary
512   layer. *Environ. Sci. Technol.* **46**, 10463–10470 (2012).

513   35.   T. a Crisp, *et al.*, Journal of Geophysical Research : Atmospheres in the polluted marine
514   boundary layer. 6897–6915 (2014).

515   36.   I. V. Patroescu, I. Barnes, K. H. Becker, FTIR kinetic and mechanistic study of the
516   atmospheric chemistry of methyl thiolformate. *J. Phys. Chem.* **100**, 17207–17217 (1996).

517   37.   X. Wang, *et al.*, The role of chlorine in global tropospheric chemistry. *Atmos. Chem. Phys.*
518   **19**, 3981–4003 (2019).

519   38.   A. D. Clarke, *et al.*, Particle nucleation in the tropical boundary layer and its coupling to
520   marine sulfur sources. *Science (80-.).* **282**, 89–92 (1998).

521   39.   C. J. Williamson, *et al.*, A large source of cloud condensation nuclei from new particle
522   formation in the tropics. *Nature* **574**, 399–403 (2019).

523   40.   P. R. Veres, *et al.*, Correction for Veres et al., Global airborne sampling reveals a
524   previously unobserved dimethyl sulfide oxidation mechanism in the marine atmosphere.
525   *Proc. Natl. Acad. Sci.* **118**, 1–3 (2021).

526   41.   P. R. Veres, J. A. Neuman, T. B. Ryerson, ATom: L2 Measurements from the NOAA ToF
527   Chemical Ionization Mass Spectrometer (CIMS)
528   https:/doi.org/https://doi.org/10.3334/ORNLDAAC/1745.

529   42.   B. Yuan, *et al.*, A high-resolution time-of-flight chemical ionization mass spectrometer
530   utilizing hydronium ions (H3O+ ToF-CIMS) for measurements of volatile organic
531   compounds in the atmosphere. *Atmos. Meas. Tech.* **9**, 2735–2752 (2016).

532   43.   J. J. Colman, *et al.*, Description of the analysis of a wide range of volatile organic
533   compounds in whole air samples collected during PEM-Tropics A and B. *Anal. Chem.* **73**,
534   3723–3731 (2001).

535   44.   G. M. Wolfe, *et al.*, Quantifying sources and sinks of reactive gases in the lower
536   atmosphere using airborne flux observations. *Geophys. Res. Lett.* **42**, 8231–8240 (2015).

537   45.   G. M. Wolfe, *et al.*, The NASA Carbon Airborne Flux Experiment (CARAFE):
538   Instrumentation and Methodology. *Atmos. Meas. Tech.* **11**, 1757–1776 (2018).

539   46.   C. Torrence, G. P. Compo, A practical guide to wavelet analysis. *Bull. Am. Meteorol. Soc.*
540   **79**, 61–78 (1998).

541   47.   P. K. Misztal, *et al.*, Airborne flux measurements of biogenic isoprene over California.
542   *Atmos. Chem. Phys.* **14**, 10631–10647 (2014).

543   48.   S. C. Wofsy, *et al.*, ATom: merged atmospheric chemistry, trace gases, and aerosols
544   (2018) https:/doi.org/https://doi.org/10.3334/ORNLDAAC/1581.
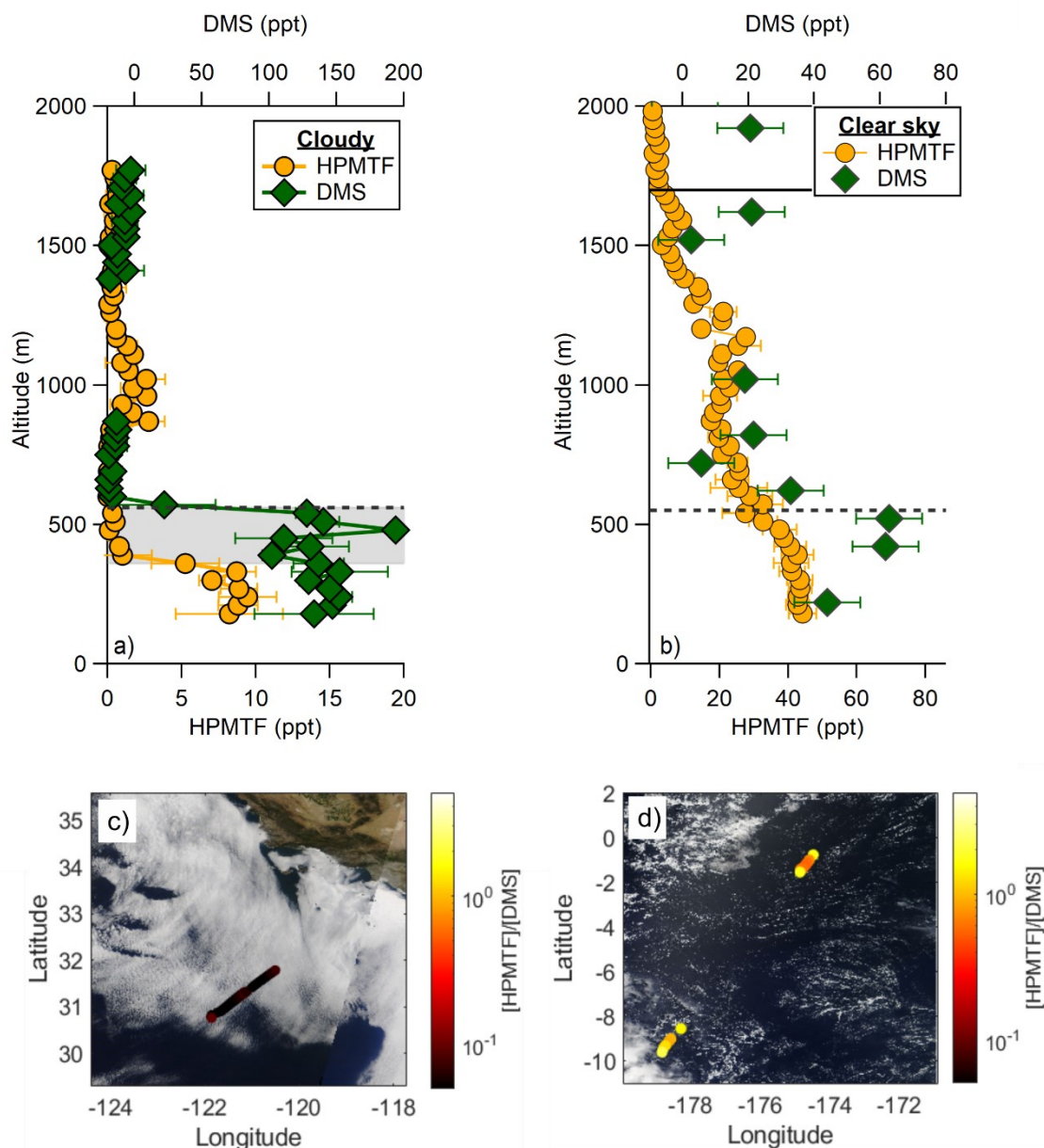
545

Figures and Tables

Figure 1. Vertical profiles of DMS and HPMTF mixing ratios under cloudy (a) and clear sky conditions (b) observed during the SARP and ATom research flights, respectively. The grey shaded region in panel (a) represents the cloudy altitudes in the marine boundary layer. The horizontal dashed lines in (a) and (b) indicate the boundary layer height. The solid line in (b) indicates the buffer layer height. The SARP vertical profile is taken from the ascent at the end of the flux period and the ATom profile is taken from the descent at the start of the second set of flux legs. Panels (c) and (d) show the research flight path colored by the observed [HPMTF]/[DMS] ratio overlaid on true color images from MODIS Terra for the SARP (c) and ATom (d) flights respectively. [HPMTF]/[DMS] in panel (c) is plotted for below cloud periods only, and for altitudes below 1500 m periods in panel (d).
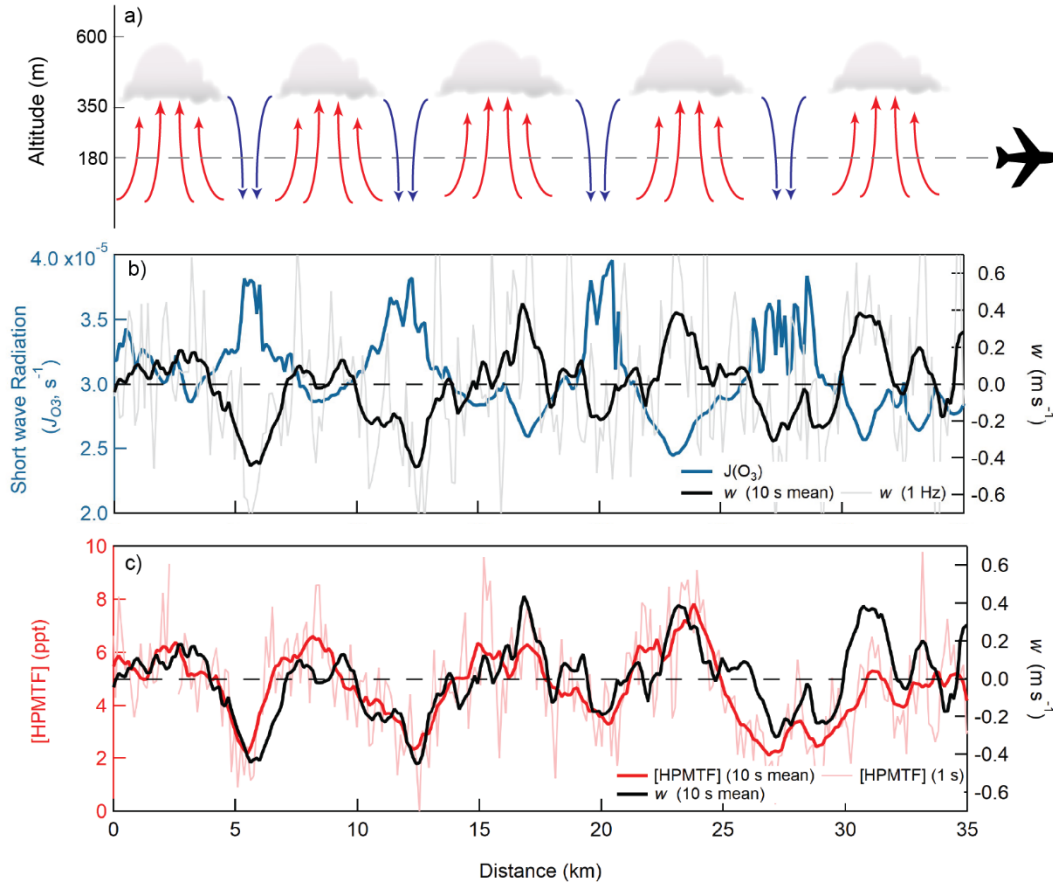
559

Figure 2. (a) Schematic of the convective roll structure observed during the SARP research flight in the cloudy marine boundary layer with periodic cloudy and clear sky regions associated with updrafts and downdrafts, respectively. (b) Time series of instantaneous vertical wind speed (w, black) and zenith ozone photolysis rates (J_{O3}, blue), proportional to downward short wave solar radiation, indicates the cloud free regions. (c) Time series of HPMTF mixing ratios ([HPMTF]) and w showing depletion of HPMTF in downdraft air parcels which have experienced cloud processing. The 10 s moving average (red) and discreet 1 s time resolution (light red) HPMTF mixing ratios are included in (c).
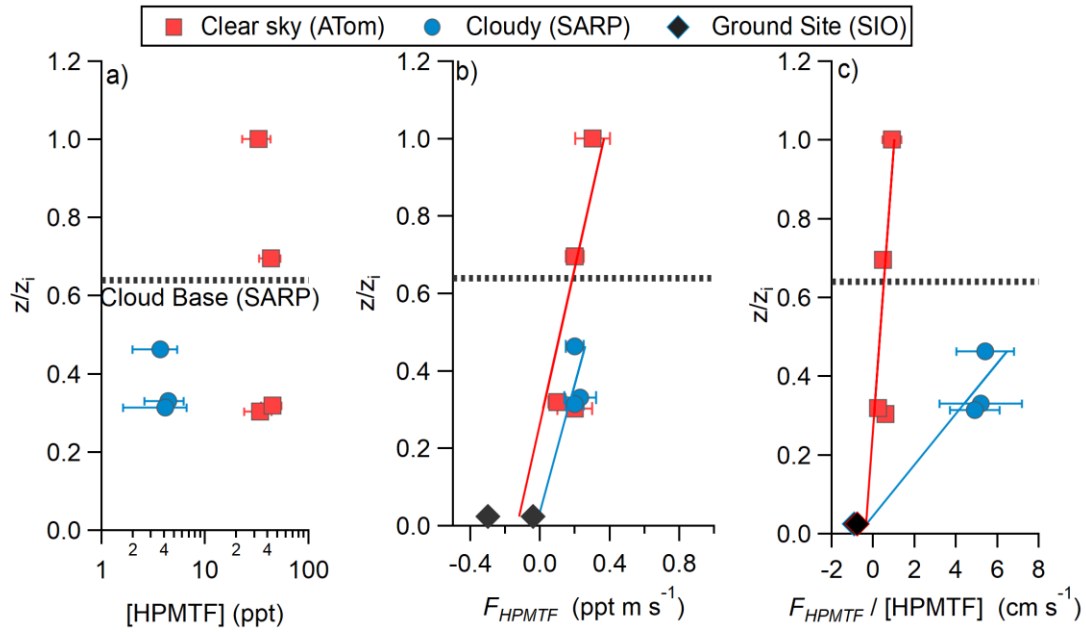
Figure 3. Observed vertical profiles of HPMTF (a) mixing ratios, (b) flux (F_{HPMTF}), and (c) flux normalized by HPMTF mixing ratios (F_{HPMTF} /[HPMTF]) observed under cloudy (blue) and clear (red) sky conditions during SARP and ATom respectively. Altitudes were normalized to the boundary layer height (z_i) during each flight. HPMTF exchange velocities measured from a coastal surface site (SIO, z = 12 m) from Vermeuel et al. (2020) were scaled to horizontal wind speed during each flight to calculate the surface flux (23). Solid lines are ordinary least square best fit lines. The dashed horizontal line on all panels indicates the height of the cloud base during the SARP flight.
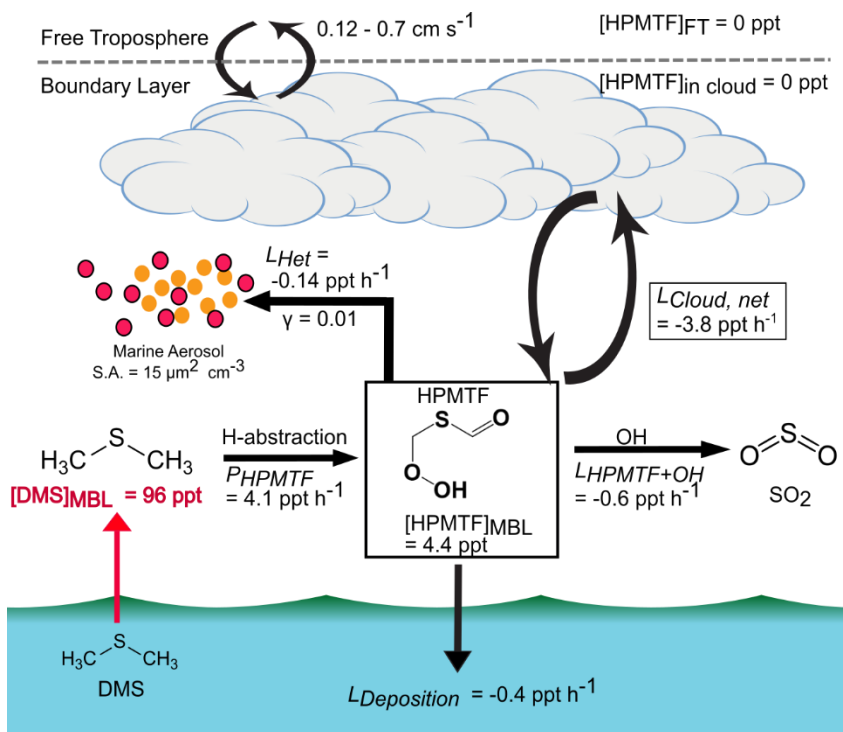
577

Figure 4. The components of the HPMTF scalar budget under cloudy sky conditions including all chemical production and loss pathways that can be directly constrained from *in-situ* observations.
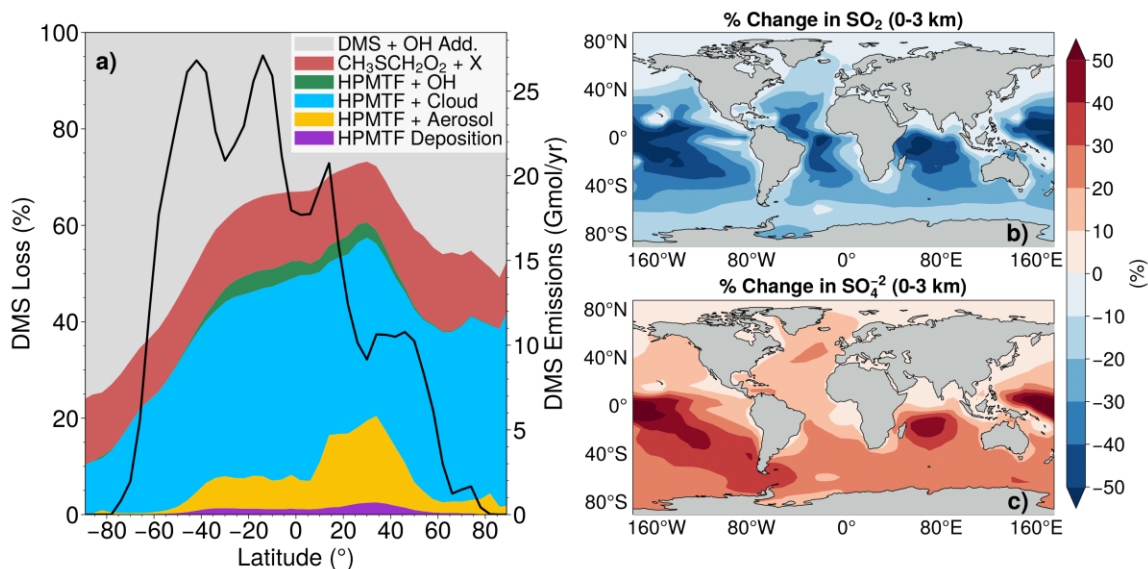
580

Figure 5. (a) Pathways for DMS removal, as simulated by GEOS-Chem: 1) OH-addition and BrO
reaction with DMS leading to MSA and SO_2 (grey), 2) H-abstraction of DMS, primarily by OH,
resulting in SO_2 production from biomolecular $CH_3SCH_2O_2\cdot$ chemistry (red). Oxidation of DMS by
Cl and NO_3 radicals are an additional minor contribution, 3) HPMTF + OH gas-phase chemistry
(dark green), 4) HPMTF irreversible uptake to clouds (blue), 5) HPMTF heterogeneous uptake to
aerosol particles (orange), and 6) HPMTF wet and dry deposition (purple). Annual mean marine
DMS emissions as a function of latitude are also shown on the right y-axis in black. Inclusion of
cloud loss and aerosol heterogeneous uptake into the HPMTF budget results in a large reduction
in [SO_2] (b) and large increase in [SO_4^{2-}] (c) for altitudes below 3 km. Results are for the model Test
Case 3. The updates to the GEOS-Chem chemical mechanism used in this model implementation
are detailed in supplemental **Table S4** and conditions for the model test cases are detailed in
supplemental **Table S5**.